



OSSOS Finds an Exponential Cutoff in the Size Distribution of the Cold Classical Kuiper Belt

J. J. Kavelaars^{1,2,3} , Jean-Marc Petit⁴ , Brett Gladman³ , Michele T. Bannister⁵ , Mike Alexandersen⁶ ,
Ying-Tung Chen⁷ , Stephen D. J. Gwyn¹ , and Kathryn Volk⁸ 

¹ Herzberg Astronomy and Astrophysics Research Centre, National Research Council of Canada, 5071 West Saanich Road, Victoria, BC V9E 2E7, Canada

JJ.Kavelaars@nrc-cnrc.gc.ca

² Department of Physics and Astronomy, University of Victoria, Elliott Building, 3800 Finnerty Road, Victoria, BC V8P 5C2, Canada

³ Department of Physics and Astronomy, University of British Columbia, 6224 Agricultural Road, Vancouver, BC V6T 1Z1, Canada

⁴ Institut UTINAM UMR6213, CNRS, Univ. Bourgogne Franche-Comté, OSU Theta F-25000 Besançon, France

⁵ School of Physical and Chemical Sciences—Te Kura Matū, University of Canterbury, Private Bag 4800, Christchurch 8140, New Zealand

⁶ Center for Astrophysics, Harvard & Smithsonian, 60 Garden Street, Cambridge, MA 02138, USA

⁷ Institute of Astronomy and Astrophysics, Academia Sinica; 11F of AS/NTU Astronomy-Mathematics Building, No. 1 Roosevelt Road, Sec. 4, Taipei 10617, Taiwan

⁸ Lunar and Planetary Laboratory, 1629 East University Boulevard, Tucson, AZ 85721-0092, USA

Received 2021 July 12; revised 2021 September 29; accepted 2021 October 1; published 2021 October 14

Abstract

The cold main classical Kuiper Belt consists of the nonresonant small solar system bodies with low orbital inclinations and orbital semimajor axes between 42.4 and 47.7 au. These objects likely formed in situ, and the population has experienced minimal collisional modification since formation. Using the Outer Solar System Origins Survey ensemble sample and characterization, combined with constraints from deeper surveys and supported by evidence from the Minor Planet Center catalog and the Deep Ecliptic Survey, we determine the absolute magnitude H_r distribution of the cold classical belt from $H_r \simeq 5$ to 12 (roughly diameters of 400–20 km). We conclude that the cold population's H_r distribution exhibits an exponential cutoff at large sizes. Exponential cutoffs at large sizes are not a natural outcome of pairwise particle accretion, but exponentially tapered power-law size distributions are a feature of numerical simulations of planetesimal formation via a streaming instability. Our observation of an exponential cutoff agrees with previous observational inferences that no large objects ($D \gtrsim 400$ km) exist in the cold population. We note that the asymptotic slope of the H_r distribution is consistent with $\alpha \sim 0.4$. This asymptotic slope is also found in streaming instability modeling of planetesimal formation and is thus not necessarily associated with achieving collisional equilibrium. Studies of the trans-Neptunian region are providing the parameters that will enable future streaming-instability studies to determine the initial conditions of planetesimal formation in the ≈ 45 au region of the Sun's protoplanetary disk.

Unified Astronomy Thesaurus concepts: [Classical Kuiper belt objects \(250\)](#); [Trans-Neptunian objects \(1705\)](#); [Kuiper belt \(893\)](#)

1. Introduction

Cold main classical Kuiper Belt objects (KBOs) appear to be unevolved products of the initial planetesimal formation process in this region of the solar system. The current number density of cold objects is such that collisions between these planetesimals are infrequent (e.g., Greenstreet et al. 2019; Abedin et al. 2021). The cold KBOs are known to contain a large number of loosely bound binary pairs (Noll et al. 2008); such pairs are very likely to be destroyed if collisions among KBOs are common (Petit & Mousis 2004), implying that the number density at the epoch of formation was similar to what we see today. The cold KBO pairs are so loosely bound that many would not have survived gravitational scattering into this zone of the solar system, implying that they formed in situ (Parker & Kavelaars 2010). Recently, observations of the cold classical KBO 486958 Arrokoth by the New Horizons mission provided direct evidence of the low collision rate in this region (McKinnon et al. 2020). Arrokoth impactors are dominantly cold classical KBOs, and the observed low crater density, well below the crater saturation threshold, is consistent with the ancient number density of material being within a factor of a few of that currently observed in this region (Greenstreet et al. 2019; Abedin et al.

2021). In addition, the photometric properties of the cold belt members appear distinct from the rest of the KBOs (e.g., Tegler et al. 2003; Pike et al. 2017; Schwamb et al. 2019). The cold objects thus provide a window into the processes of planetesimal formation.

An examination today of the H_r (absolute magnitude) distribution of cold objects larger than 20 km may provide a direct measurement of the distribution that emerged from the initial planetesimal formation processes. This population, unlike the collisionally evolved asteroid belt, never experienced the runaway growth to proto- or dwarf planets, experienced minimal collisional erosion, and has dynamical and surface properties that are distinct from the rest of the KBOs. The cold KBO mass function today is the most likely to resemble the initial mass function of planetesimals.

The outcomes of planetesimal formation modeling are reaching a point where guidance from rigorous observational constraints are needed. The mass range in current model outputs overlaps with the well-observed range probed by the Outer Solar System Origins Survey (OSSOS). Here we present the high-fidelity measurement of the absolute magnitude distribution of the observed cold classical Kuiper Belt as determined from an ensemble of survey samples (Kavelaars et al. 2009; Petit et al. 2011, 2017; Alexandersen et al. 2016;

Bannister et al. 2018) and associated detection characterizations (hereafter referred to as OSSOS++).

2. The OSSOS++ Cold Belt Absolute Magnitude Distribution

From the OSSOS++ sample (see Table 3 of Bannister et al. 2018 for full details), we select the 321 objects with a free inclination $i_{\text{free}} < 4^\circ$ and semimajor axis in the range $42.4 \text{ au} < a < 47.7 \text{ au}$ to provide a relatively clean sample of the properties of cold main classical KBOs. Van Laerhoven et al. (2019) found the orbital parameter that best separates the cold population from the background of the main classical Kuiper Belt is the inclination with respect to the a -dependent Laplace plane, i.e., i_{free} , and that $i_{\text{free}} < 4^\circ$ provides a reasonable split between the cold and excited populations. The $39.9 \text{ au} \lesssim a \lesssim 42.4 \text{ au}$ zone is usually included in the nominal definition of the main classical Kuiper Belt. This zone, however, was likely destabilized by the passage of the ν_8 resonance during Neptune migration, and KBOs on low- i orbits would have been removed. The few low- i_{free} KBOs in this zone today are unlikely to have formed in situ, and for that reason, we exclude them when considering the cold classicals. Our sample criterion may exclude a small number of cold members from our analysis but ensures minimal contamination from other populations that may not have formed in situ and would distort the view of the unevolved H_r distribution.

2.1. Sample Characterization

Using the OSSOS++ characterization (Bannister et al. 2018), we debias the orbit and H_r distributions of detected objects. The low eccentricity of the cold KBO orbits results in these objects exploring a limited range of solar distances within a constrained phase-space volume. As a result of this constraint, the OSSOS++ sample of cold objects provides a complete sampling of the orbit distribution (there are no hidden or unseen populations), and we can robustly debias the detected sample. We consider the four-dimensional phase space $(a, q, \sin(i_{\text{free}}), H_r)$ and slice it into cells small enough (0.2 au, 0.2 au, 0.001, 0.1) such that the distribution of elements within a cell is likely uniform (see Figure 5 of Bannister et al. 2018 for the distribution of these elements). To determine the detection bias, we create model objects that uniformly sample each cell’s parameter range and use the OSSOS survey simulator (Lawler et al. 2018a) to determine the fraction that would have been detected by the OSSOS++ surveys. For each element cell k , the detection bias, \mathcal{B}_k , is the number of simulated orbits detected in that cell divided by the number of orbits drawn from the cell. For each cell, we simulated the detection of 5000 objects by OSSOS++, and the value of \mathcal{B}_k is 5000 divided by the number of draws from the model needed to achieve the 5000 simulated detection. For the cold main classical belt, the values of the bias range from $\mathcal{B}_k \simeq 1/10$ for $H_r \simeq 5.5$ objects near the inner boundary of the classical region to $\mathcal{B}_k \simeq 1/100$ for the $H_r \simeq 8.3$ objects near the outer exterior of the classical region. Although we computed bias factors for objects with larger H_r values, we do not use those in our analysis, as the bias correction factors grow rapidly near the limit of detection. For each of the observed cold objects in the sample, we determine the element cell, k , the detection belongs to and add $1/\mathcal{B}_k$ objects to our model, with the specific elements of those model objects drawn randomly

across the cell’s element distribution. Using this procedure provides an estimate of the number of objects in the cold population required to generate the OSSOS++ detections and the distribution of the population over each of the orbit and absolute magnitude $(a, q, \sin(i_{\text{free}}), H_r)$ parameters. Figure 1 presents the resulting OSSOS++ cumulative H_r distribution.

2.2. Other Observational Constraints

We compare with other cold KBO samples to verify our total population estimates at both the faint and bright ends of the H_r distribution. Determination of population statistics requires carefully tracking each detected object to ensure that the orbit is accurately determined and the object is correctly classified. This tracking requires significant investment in telescope time if one is to avoid ephemeris bias entering the sample (Jones et al. 2006; Kavelaars et al. 2008). This also places a significant constraint on the faintness of objects that are allowed into a particular survey, as the cost of tracking will rapidly increase. The OSSOS++ sample provides a high-quality sampling of the cold Kuiper Belt due to the nearly 100% effectiveness in tracking detections to obtain high-quality orbits. The desire to achieve this high success rate in tracking, however, also limited the flux range accessible to the survey at both the bright and faint ends of the H_r distribution. Other surveys that do not have precise orbit and distance estimates for all of their objects, however, can be used to estimate the cold classical H -magnitude distribution and extend the flux range explored. We find that these additional samples agree well with the results measured via the OSSOS++ sample, providing a verification of the absolute calibration of our study.

2.2.1. Deep Studies

Gladman et al. (2001), Bernstein et al. (2004), Fraser et al. (2008), Fuentes & Holman (2008), and Fraser & Kavelaars (2009; hereafter G01, B04, Fr08, FH08, and FK09) performed deep “pencil-beam” surveys to detect faint trans-Neptunian objects and published their detection efficiency functions. The imprecise determination of heliocentric distance at detection in G01, Fr08, FH08, and FK09, however, prevents direct conversion from observed brightness to H_r (absolute) magnitudes. We carefully examined the sample of detections from each of these projects. The Very Large Telescope part of G01 did not yield any detections, and we keep only the CFHT component of that project (G01/CFHT). The inclinations in the Blanco part of Fr08 are insufficiently constrained to select cold objects from the sample; thus, we utilized only the CFHT component from that project (Fr08/CFHT). The details provided in FH08 and FK09 are sufficient to allow use of their full sample of detected cold KBOs. For each survey, we examined the published detection efficiency curves and determined the limiting apparent magnitude M_r (all surveys used here reported limits in r) up to which the efficiency of detection, η , is roughly constant (see Table 1). For each survey, we

1. count the number n of cold objects (estimated⁹ inclination $\leq 4^\circ$) brighter than M_r ;
2. estimate the actual number of objects present in the field of view of the survey and brighter than M_r as n/η ;

⁹ We cannot compute i_{free} as the semimajor axes of the orbits of the objects are, generally, unknown.

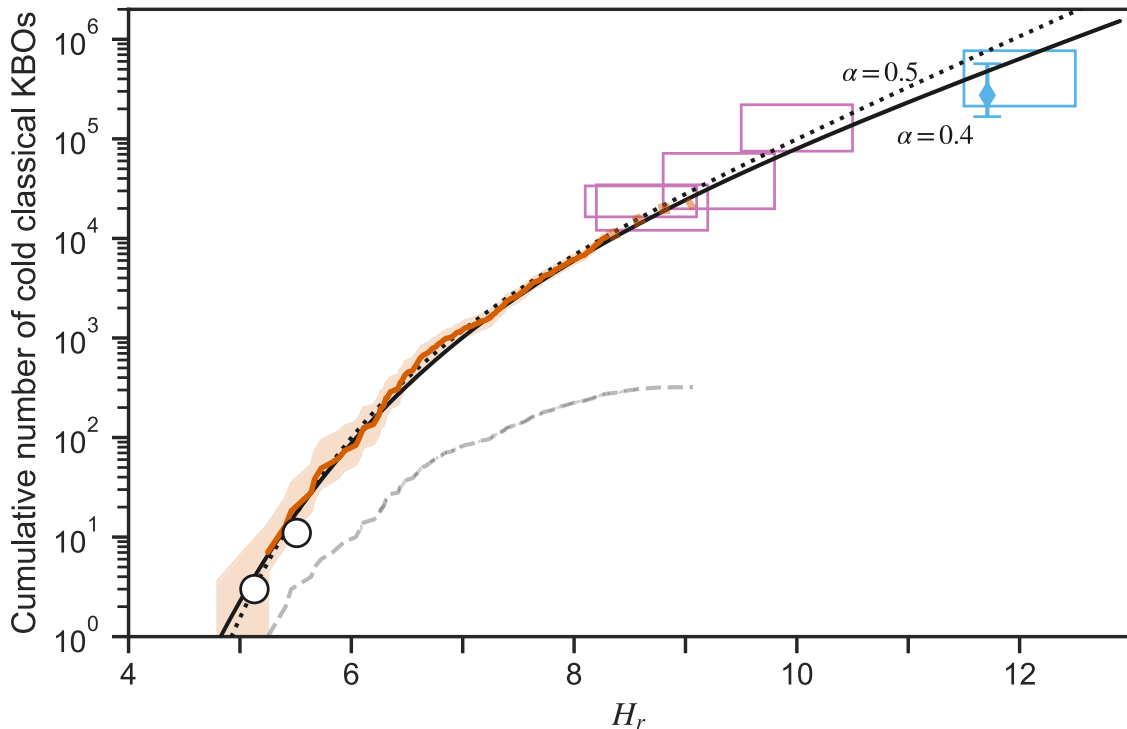


Figure 1. The H_r distribution of the cold main Kuiper Belt. The gray dashed line represents the distribution of raw detections in the OSSOS++ sample. The orange curve (shown as a dotted line for $H_r > 8.3$, where our sample debiasing is less secure) represents the debiased OSSOS++ sample, with the shading indicating the Poisson 95% confidence range. The black lines represent two exponentially tapered functions matched (see Section 3) to the debiased OSSOS++ data with forced large- H_r (small object) asymptotic slopes (dotted: $\alpha = 0.5$; solid: $\alpha = 0.4$). For $H_r < 9$, the two model curves are nearly identical. The debiased OSSOS++ measurements are well matched by the exponential taper form. The boxes represent literature-derived estimates; see Table 1 and Section 2.2.1. The cyan diamond with uncertainty represents a direct debiasing of detected cold classical in B04. The black open circles are located where the MPC database indicates a cumulative total of 3 ($H_r \sim 5.13$) and 11 ($H_r \sim 5.51$) main-belt cold objects.

3. determine the fraction of the full cold population that is in the field of view of a survey at any given time, F , using the CFEPS orbit model (Petit et al. 2011); and
4. compute an estimate of the implied full population brighter than M_r : $N(m < M_r) = n/(F\eta)$.

The 95% confidence range for N is computed from the 95% Poisson confidence range for n and listed as N_- for the lower end of the confidence range and N_+ for the upper in Table 1. To add these density estimates to our H_r distribution, we must convert the observed apparent magnitude limit (M_r) to an absolute (H_r) value, which requires knowledge of the distance to the sources. As the precise distances of the individual detections are not known, we determine a plausible range of H_r values by adopting the 95% range of distances of the cold objects from the CFEPS model (Petit et al. 2011; Fraser et al. 2014; 40.3–51 au). Using this approach, we determine $H_r(51)$ and $H_r(40.3)$ (using $H_{51} = M_r - 17.03$ and $H_{40.3} = M_r - 16.00$) as representative of the range of H_r values that each survey was sensitive to at the detection limit (M_r).

Authors B04 provided precise distance estimates and even rough orbital elements and the characterization of the detection efficiency. Thus, for B04, we also debiased the three detections of that survey following the same procedure as for OSSOS++. For B04, the full debiasing results in a population estimate at the largest H_r of the detected B04 objects that is compatible with the estimate using the process outlined in the preceding paragraph (Figure 1).

We discuss the implications for the observed H_r distribution in Section 3.

2.2.2. Inventory of the Brightest Cold Classicals

The now nearly complete, and sparse, inventory of the lowest H (largest) cold classical KBOs provides a further constraint on the size distribution. We select from the Minor Planet Center (MPC) database KBOs consistent with the a and i_{free} cuts given above and precise orbits (two oppositions or more, six observations or more, and an MPC orbit uncertainty parameter less than or equal to 6). The MPC database provides the visual absolute magnitude H , which we convert into H_r using $\langle H - H_r \rangle = 0.19$, the mean value for the cold objects from OSSOS++ present in the MPC database. We then determine the number of known cold classical KBOs with $H_r < 5.1$ (3) and 5.5 (11) and include this as an estimate of the cumulative H_r distribution; see Figure 1. These MPC-derived population estimates are nearly identical to the OSSOS++-based estimate of the total numbers at these H_r values, confirming the global population estimates obtained by our debiasing. That the OSSOS++ estimate of the total population of cold objects is the same size as the currently known sample suggests that, as previously noted (e.g., Sheppard et al. 2011), the MPC database has reached (near) completeness for H around 5–6 mag. The expectation that the brightest members of the cold population would be in this range was also noted in Figure 7 of Bernstein et al. (2004) and is apparent in Figure 9 of Fraser et al. (2014). The expectation of completeness in the MPC sample is also coherent with the reported detection of large cold objects by Pan-STARRS, which surveys the whole ecliptic. During the period 2010–2014, Pan-STARRS found seven of the 20 largest objects in the cold belt region defined

Table 1
Deep Luminosity Function Surveys

Survey ^a	η	M_r	n_{cold}	$1/F$	H_{51}	$H_{40.3}$	N_-	N_+
Fuentes & Holman (2008)	0.88	25.1	30	930	8.1	9.1	22,300	45,300
Fraser et al. (2008) CFHT	0.97	25.2	11	1726	8.2	9.2	11,000	35,000
Gladman et al. (2001) CFHT	1.00	25.8	3	11,700	8.8	9.8	10,733	94,100
Fraser & Kavelaars (2009)	0.95	26.5	10	11,594	9.5	10.5	67,000	224,500
Bernstein et al. (2004)	1.00	28.5	3	115,325	11.5	12.5	125,700	1,011,100

Note.

^a If a telescope is listed, the sample is restricted to that particular portion of the study.

above. Since 2014, no new large cold objects have been reported by Pan-STARRS, despite continuous operation. An absence of $H_r < 4$ cold objects was also predicted a decade ago based on the CFEPS project (see Section 5.1.1 of Petit et al. 2011), whose sample is included in OSSOS++. The total inventory of known cold population objects with $H_r < 5.5$ precisely matches the prediction from the OSSOS++ H_r distribution, appears to be complete, and is small in number.

3. An Exponentially Tapered H_r Distribution

The shape of the cold population H_r distribution presented in Figure 1 is inconsistent with two-component power-law¹⁰ fits. Using our debiased model, we imposed various two-component power laws (see Fraser et al. 2014) onto our model and compared the resulting orbit and H_r distributions with our observed sample. No acceptable models (rejected by the AD test statistic at more than 99% confidence; see Lawler et al. 2018a for details of our statistical procedure) were found. Moving to a multicomponent power law could provide a solution but is difficult to physically motivate. The shape is also not consistent with the rolling power law utilized in Bernstein et al. (2004). The steep and continuously evolving shape at the bright end of the H_r distribution is inconsistent with these representations.

A tapered power-law form appears to be emerging as a preferred functional form for planetesimal mass distributions. Disk instability mechanisms, and the streaming instability (SI) process in particular, have recently become highly favored solutions to overcoming various physical barriers in planetesimal formation (e.g., Safronov 1972; Johansen et al. 2007; Lyra & Umurhan 2019) and enable planetesimal formation to proceed more rapidly at lower surface densities, like those in the primordial cold Kuiper Belt. Independent groups have investigated the initial mass function of planetesimals resulting from the SI (Johansen et al. 2015; Simon et al. 2016; Schäfer et al. 2017; Abod et al. 2019; Li et al. 2019; Liu et al. 2020; Rucska & Wadsley 2021). Due to limitations in the simulated mass resolution, the low-mass end of the mass function that emerges from SI models is not strongly constrained. The existing works, however, exhibit similar-shaped mass distributions that a power law can roughly approximate at the small-mass end but require a rather sharp exponential cutoff at the large-mass end. Several functional forms to fit the mass distributions have been proposed. We select the exponentially

(Schäfer et al. 2017) or variably (Li et al. 2019) tapered power-law form. According to the Bayes criterion, these forms provide better matches to the SI outcomes than simpler, single-parameter functions (Schäfer et al. 2017; Li et al. 2019).

The exponentially tapered power-law mass distribution (Schäfer et al. 2017) can be transformed into an H_r distribution assuming a constant albedo, density, and spherical shape:

$$N(<H_r) = 10^{\frac{3}{5}\alpha_{\text{SI}}(H_r - H_o)} \exp[10^{-\frac{3}{5}\beta_{\text{SI}}(H_r - H_B)}], \quad (1)$$

where N will be the total population number, H_o is a normalization, α_{SI} is the asymptotic slope at large H_r , β_{SI} is the strength of the exponential tapering, and H_B is the H_r value at which the exponential taper begins to dominate. The α in the single exponential H_r distribution, $N(<H_r) = 10^{\alpha(H_r - H_o)}$, is given by $\alpha = \frac{3}{5}\alpha_{\text{SI}}$ and can be seen as related to the faint/small object exponent when considering multicomponent exponential distributions.

The OSSOS++ sample confirms the general shape of an exponential taper and can be used to determine the strength of that tapering (β_{SI}). The OSSOS++ sample is, however, limited to the large- H_r end, where our debiasing factors are small; the value of α_{SI} is not robustly constrained by the OSSOS++ sample. Crater counts on Pluto and Charon (Singer et al. 2019a), the observed sizes of Jupiter-family comets (Solontoi et al. 2012), and results from deep surveys shown in Figure 1 indicate that $\alpha \simeq 0.3$ – 0.5 faintward of $H_r \sim 9$. In Figure 1, we present fits of Equation (1) with fixed values of $\alpha \in \{0.4, 0.5\}$ ($\alpha_{\text{SI}} \in \{0.66, 0.83\}$), with the value of β_{SI} and the other free parameters determined using maximum-likelihood Markov Chain Monte Carlo parameter exploration via the *emcee* package (Foreman-Mackey et al. 2013) over the range $H_r \in \{5.0, 8.3\}$. The OSSOS++ estimates of $\beta_{\text{SI}} \in \{0.42_{-0.16}^{+0.12}, 0.59_{-0.27}^{+0.13}\}$, $H_o \in \{-2.6_{-0.9}^{+0.4}, 0.0_{-0.4}^{+0.2}\}$, and $H_B \in \{8.1_{-0.6}^{+1.7}, 7.1_{-0.4}^{+0.9}\}$ provide a remarkably smooth match to our debiased observations, and our estimates of the value of β_{SI} are steeper than but consistent with the range of values found in SI modeling (0.28–0.37; e.g., Schäfer et al. 2017).

3.1. Comparison with Published Distributions

Figure 2 presents our measured debiased H_r distribution along with a number of results from the literature. The double or broken exponential forms presented in Figure 2 do not provide as compelling a match to the observations as the tapered exponential. There is good agreement that the asymptotic small object exponential must be around $\alpha \sim 0.4$, but the forms do not provide a good match to the data at small H_r , which exhibits a continuously steepening slope. The OSSOS++ data are consistent with the bright end exponential slopes over some limited range of H_r , then drop away from

¹⁰ We sometime use the term power law to refer to the exponential forms, such as $N(<H) \propto 10^{\alpha H}$, as the underlying mass distribution is, in fact, a power-law form, and H is used as a proxy for that quantity, and referring to exponentially tapered exponential functions becomes exponentially confusing but does reflect the exponential complexity of reality.

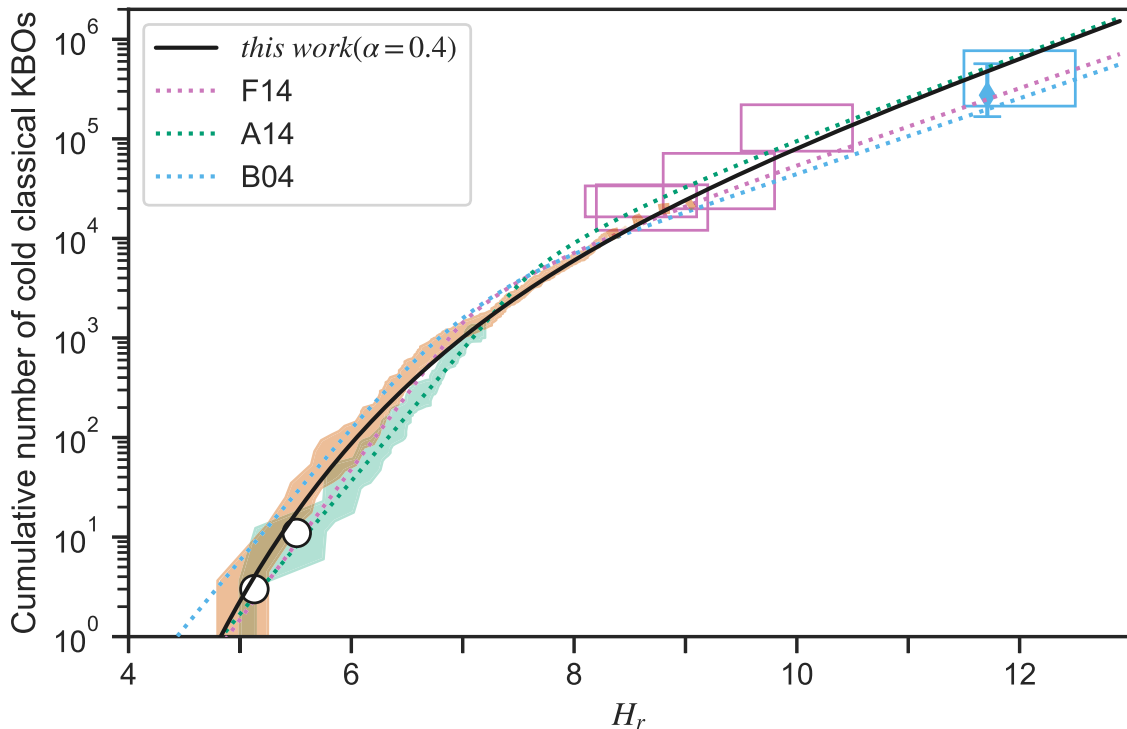


Figure 2. As in Figure 1, the orange region represents the debiased OSSOS++ sample. The green shaded area represents the debiased detections from the Deep Ecliptic Survey (Adams et al. 2014), with the green dotted line indicating the best-fit double exponential. Also shown are the best fits from Bernstein et al. (2004; cyan dotted line) and Fraser et al. (2014; magenta dotted line). The curves have been scaled to reflect the difference in survey filters and for differences in selection function for cold classical KBOs. In particular, we use $(r - R) = 0.25$ (Jordi et al. 2006) for $(V - R) = 0.6$ cold classical KBOs, and we scale the apparent magnitude distribution given in B04 using a fixed distance of 42 au to transform from r to H_r . The A14 total population is slightly low compared to the OSSOS++ sample; this may be due to tracking losses reported in A14. The F14 fit has been scaled to match the OSSOS++ sample at $H_r = 8$, as we were uncertain of the scaling from the surface density reported in F14 and the absolute total numbers reported here.

those curves for both smaller and larger H_r . The bright/large object end of the H_r distribution is not a single sloped value; thus, double exponential functions are not a good match.

4. Discussion

The H_r distribution of the OSSOS++ sample clearly demonstrates an exponentially tapered shape. OSSOS was designed to be an absolutely calibrated survey that could be debiased to measure intrinsic absolute distributions inside each dynamical group, with the group membership based on high-precision orbits. These orbits permit the computation of free inclinations and the exclusion of resonant objects enabling the selection of a relatively uncontaminated sample of cold belt members. We find that the debiased H_r distribution of this sample is inconsistent with a single power law at the bright end (see Figures 1 and 2). The functional form of the cold-component H_r distribution is well represented by an exponential taper of the type seen in numerical simulations of SI-driven planetesimal formation.

The OSSOS++-derived H_r distribution matches well with independent constraints at both ends of the distribution. At the faint (large- H_r) end, the debiased OSSOS++ sample connects smoothly to the faintest pencil-beam studies. Although each individual study is difficult to map to a precise $N(<H_r)$ value, the ensemble of deep apparent magnitude studies collectively matches OSSOS++, implying that the asymptotic form of a single exponential from $H_r > 9$ down to at least $H_r \approx 12$ does not violate known constraints. The cratering records on Pluto and Charon (Robbins et al. 2017; Singer et al. 2019a) and Arrokoth (Spencer et al. 2020), however, indicate at least one further transition to an even shallower exponent beyond

$H_r > 17$. The OSSOS++ sample provides strong constraints in the $H_r \approx 5$ –8.3 range; for $H_r > 8.3$, where our detected sample drops off, a constant slope in log-space appears plausible for several more magnitudes. We highlight that within the hot component, there is evidence for a knee or divot (Shankman et al. 2013, 2016; Alexandersen et al. 2016) feature near $H_r = 8.5$ with a similar shallow slope for $H_r > 9$. On the large object end, the cumulative distribution of the intrinsically brightest known cold classical KBOs falls directly on the OSSOS++ curve and its brightward extrapolation. This close match confirms the very steep nature of the H -magnitude distribution of the largest objects and implies that the inventory of these largest objects is essentially complete. These connections to independent constraints at $H_r = 5$ and 9 (with no tuning) give confidence that in OSSOS++, we have an absolutely calibrated survey, and that the H -magnitude distribution’s shape between these two ends is correctly represented by our debiased measurement.

The existence of the exponential taper also resolves some literature confusion regarding the measured exponent of the KBO H_r distribution. Much of the historical literature fit a single exponential to the apparent magnitude $N(<M) \propto 10^{\alpha M}$. Because of the finite sky area and the small number of objects detected in any given survey, even fitting a simple exponential was challenging due to a lack of dynamic range. Generally, larger-area surveys were shallower, while deeper surveys made up for their smaller area via the steep H_r distribution to end up with comparable (but small) samples. Magnitude distribution shape estimates done in apparent magnitude space (because they lack the precise distance estimates required to translate

apparent to absolute magnitude) “blur” the H -magnitude distribution, resulting in slope estimates that are a function of the depth of the survey; a similar conclusion was reached in Fraser et al. (2014).

Papers that attempted to combine surveys to enlarge the apparent magnitude and dynamic range of observational constraints tended to average this out to an intermediate slope (e.g., Gladman et al. 1998; Fraser et al. 2008). With an even larger apparent magnitude range, it became clear that a single exponential could not represent the data, and double/rolling exponent forms were introduced. Magnitude distribution studies near the solar system’s invariable plane (which are thus dominated by low-inclination cold-component objects) exhibited a change of α to shallower values fainter than $m_r \simeq 24\text{--}25$ (thus $H_r \sim 8\text{--}9$ in the main belt) when using rolling (Bernstein et al. 2004), double (Fuentes et al. 2009), or broken (Fraser & Kavelaars 2009) power-law size distributions.

Although computationally convenient, there is no physical motivation for a broken power law being the correct functional form. Numerical simulations of the SI, however, appear to naturally produce the exponentially tapered form (Schäfer et al. 2017; Li et al. 2019). The OSSOS++ sample demonstrates that this functional form is an excellent representation of the cold-component H -magnitude distribution. Much of the discussion of what value of α best matches the actual H_r distribution and where to put a break to attempt to mimic the slope evolution appears to be due to trying to model an exponential taper by combining multiple exponential distributions.

Having such examples of the danger of overimposing a functional form on reality, we note that although this tapered exponential is clearly impressively similar to the distribution derived from the OSSOS++ sample, numerical simulations (e.g., Li et al. 2019) show that there can be smaller features superposed on this dominant form that, in differential space, manifest themselves as local “knees” (broken or double exponents) or “divots” (Shankman et al. 2013). In particular, the weak relative underabundance just past $H_r \simeq 7$ present in previous data sets (e.g., Adams et al. 2014; Fraser et al. 2014) may be real, in addition to a proposed knee near $H_r \simeq 8.4$ in the dynamically hot populations (e.g., Alexandersen et al. 2016; Lawler et al. 2018b).

The SI modeling prediction of the shape of the H -magnitude distribution at small sizes (large H) is not yet firmly established. The value of the asymptotic power-law slope seen at small sizes in simulations (Simon et al. 2017, 2016; Abod et al. 2019; Rucska & Wadsley 2021) may result from resolution effects. Li et al. (2019) demonstrated that as resolution is improved, what initially appeared to be a rollover to a “single- α ” asymptotic form continues to evolve, and the transition to the asymptotic form appears to occur at ever smaller sizes. Interestingly, the existing estimates of these asymptotic limits (see Figure 10 in Abod et al. 2019, for example) are not very far from the often-suggested value of $\alpha \simeq 0.4 \pm 0.1$ for $H_r \gg 8$ (Bernstein et al. 2004; Fuentes & Holman 2008; Fraser et al. 2010, 2014). This allows for the possibility that this value of α is then set by the formation size distribution, and the similarity of the observed H_r distribution slope to the collisional equilibrium value is not evidence of collisional equilibrium having been achieved. The small object size distribution of the cold classical Kuiper Belt appears to be unaltered over the age of the solar system and to

preserve a shape consistent with SI planetesimal formation down to of order kilometer scale.

The comparison with current modeling of SI-driven planetesimal formation is not, however, without a significant hurdle. Although the shape of the distribution is compelling, the inferred mass ranges are not a good match. If the current cold component is indeed a relatively unevolved population, then the current surface density may be taken as a proxy of the density at formation. Based on our estimate of the total cold population (Figure 1), we can infer the surface density at the time of the SI process. To estimate this density, we convert our H_r distribution to a mass distribution by assuming a constant albedo of 0.15 and an object bulk density of 500 kg m^{-3} (Spencer et al. 2020) and then spread the inferred total mass into a 2 au wide ring centered at 43 au. The resulting estimated primordial surface density in solids is $\Sigma_p \sim 5 \times 10^{-5} \text{ g cm}^{-2}$. This is 100 times lower than the mass scale required for most SI modeling to produce $D \sim 400 \text{ km}$ objects (e.g., Abod et al. 2019). The number densities inferred from the current population are far too low to be consistent with SI processes forming the sizes of KBOs in our observed size distribution, which we claim follows the shape seen in SI modeling. Conversely the number density at the time of planetesimal formation implied by SI modeling results appears to be significantly higher than that inferred from the currently observed population.

There appear to be at least the following possible issues to consider.

1. The current density could be many factors lower than that at the time of planetesimal formation. This appears unlikely, as any process that removed significant mass would very likely have disrupted the binary KBO population we see today. The cratering record seen on Arrokoth is fully consistent with the low total populations reported here (see Greenstreet et al. 2019; Singer et al. 2019b; Abedin et al. 2021), indicating that any period of high number density would have been very rapidly removed, which would have implications for the orbit distribution in the cold belt (Gladman & Volk 2021). Thus, it appears unlikely that the surface density at $\sim 43 \text{ au}$ was significantly higher than today.
2. The SI process is not directly responsible for the production of the objects we see today; instead, they formed after the SI process via particle–particle interactions. A 2 au wide ring would contain many hundreds to thousands of SI cells (e.g., Li et al. 2019), and perhaps the planetesimals from these cells coalesce to form the largest bodies. Here again, the currently observed density makes this appear improbable, as the inferred particle–particle encounter rate would be very low (thus the low number of craters), making the rate of planetesimal growth so slow that the largest objects would not yet have formed. In addition, there is no reason that the observed H_r distribution of the postgrowth populations would then so closely resemble that which emerged from the SI processes.
3. The models of SI are incomplete, and the process happens on scales and at densities that have not yet been fully modeled. This appears unlikely to be the case, as the modeling is done in scale-free units, and then the mass scales are set by imposing a density.

4. The classical Kuiper Belt was much more tightly confined, radially and azimuthally, at the time of SI-driven planetesimal formation and then rapidly dispersed shortly after the planetesimals emerged. This ad hoc solution has some appeal, as many planet-forming disks exhibit density enhancements (e.g., van der Marel et al. 2013), and the shearing out of particles that might form in such dense regions would be quite rapid compared to collisional timescales. To achieve the required density enhancement, however, would require a concentration that is 100 times that seen today. Are such density enhancements feasible?

Some caution is thus warranted, because what is observed today in the cold classical Kuiper Belt is, in this paradigm, the end state of SI plus later accretion and erosion. If the latter two processes are indeed negligible (or could be successfully modeled), then the shape of the cold classical belt H -magnitude distribution becomes a direct measure of the outcome of the planetesimal formation process from the SI. Future numerical work can then, in principle, constrain the protoplanetary disk's parameters (surface density, viscosity, etc.) as one targets reproducing the observed distribution in the preserved cold classical belt.

Regardless of a possible link with the SI process, our analysis of the OSSOS++ sample has provided a robust high-fidelity measure of the H_r distribution of the cold component of the Kuiper Belt. This analysis is enabled by the precise characterization of the OSSOS++ surveys. The derived shape exhibits an exponentially tapered form and, from the current evidence, is representative of the initial distribution resulting from planetesimal formation.

J.J.K. and B.G. acknowledge the support of the Natural Sciences and Engineering Research Council of Canada. This work was supported by the Programme National de Planétologie (PNP) of CNRS-INSU cofunded by CNES. This research made use of the Canadian Advanced Network for Astronomy Research (CANFAR) and the facilities of the Canadian Astronomy Data Centre operated by the National Research Council of Canada with the support of the Canadian Space Agency. K.V. acknowledges support from NASA (grants NNX15AH59G and 80NSSC19K0785) and the NSF (grant AST-1824869). Based on observations obtained with Mega-Prime/MegaCam, a joint project of CFHT and CEA/DAPNIA, at the Canada–France–Hawaii Telescope (CFHT), which is operated by the National Research Council (NRC) of Canada, the Institut National des Sciences de l'Univers of the Centre National de la Recherche Scientifique (CNRS) of France, and the University of Hawaii. The observations at the CFHT were performed with care and respect from the summit of Maunakea, which is a significant cultural and historic site.

ORCID iDs

J. J. Kavelaars <https://orcid.org/0000-0001-7032-5255>
 Jean-Marc Petit <https://orcid.org/0000-0003-0407-2266>
 Brett Gladman <https://orcid.org/0000-0002-0283-2260>
 Michele T. Bannister <https://orcid.org/0000-0003-3257-4490>
 Mike Alexandersen <https://orcid.org/0000-0003-4143-8589>

Ying-Tung Chen <https://orcid.org/0000-0001-7244-6069>
 Stephen D. J. Gwyn <https://orcid.org/0000-0001-8221-8406>
 Kathryn Volk <https://orcid.org/0000-0001-8736-236X>

References

- Abedin, A. Y., Kavelaars, J. J., Greenstreet, S., et al. 2021, *AJ*, **161**, 195
 Abod, C. P., Simon, J. B., Li, R., et al. 2019, *ApJ*, **883**, 192
 Adams, E. R., Gulbis, A. A. S., Elliot, J. L., et al. 2014, *AJ*, **148**, 55
 Alexandersen, M., Gladman, B., Kavelaars, J. J., et al. 2016, *AJ*, **152**, 111
 Bannister, M. T., Gladman, B. J., Kavelaars, J. J., et al. 2018, *ApJS*, **236**, 18
 Bernstein, G. M., Trilling, D. E., Allen, R. L., et al. 2004, *AJ*, **128**, 1364
 Foreman-Mackey, D., Hogg, D. W., Lang, D., & Goodman, J. 2013, *PASP*, **125**, 306
 Fraser, W. C., Brown, M. E., Morbidelli, A. R., Parker, A., & Batygin, K. 2014, *ApJ*, **782**, 100
 Fraser, W. C., Brown, M. E., & Schwamb, M. E. 2010, *Icar*, **210**, 944
 Fraser, W. C., & Kavelaars, J. J. 2009, *AJ*, **137**, 72
 Fraser, W. C., Kavelaars, J. J., Holman, M. J., et al. 2008, *Icar*, **195**, 827
 Fuentes, C. I., George, M. R., & Holman, M. J. 2009, *ApJ*, **696**, 91
 Fuentes, C. I., & Holman, M. J. 2008, *AJ*, **136**, 83
 Gladman, B., Kavelaars, J. J., Nicholson, P. D., Lored, T. J., & Burns, J. A. 1998, *AJ*, **116**, 2042
 Gladman, B., Kavelaars, J. J., Petit, J.-M., et al. 2001, *AJ*, **122**, 1051
 Gladman, B., & Volk, K. 2021, *ARA&A*, **59**, 203
 Greenstreet, S., Gladman, B., McKinnon, W. B., Kavelaars, J. J., & Singer, K. N. 2019, *ApJL*, **872**, L5
 Johansen, A., Mac Low, M.-M., Lacerda, P., & Bizzarro, M. 2015, *SciA*, **1**, 1500109
 Johansen, A., Oishi, J. S., Mac Low, M.-M., et al. 2007, *Natur*, **448**, 1022
 Jones, R. L., Gladman, B., Petit, J. M., et al. 2006, *Icar*, **185**, 508
 Jordi, K., Grebel, E. K., & Ammon, K. 2006, *A&A*, **460**, 339
 Kavelaars, J., Jones, L., Gladman, B., Parker, J. W., & Petit, J. M. 2008, in *The Solar System Beyond Neptune*, ed. M. A. Barucci et al. (Tucson, AZ: Univ. Arizona Press), 59
 Kavelaars, J. J., Jones, R. L., Gladman, B. J., et al. 2009, *AJ*, **137**, 4917
 Lawler, S. M., Kavelaars, J. J., Alexandersen, M., et al. 2018a, *FrASS*, **5**, 14
 Lawler, S. M., Shankman, C., Kavelaars, J. J., et al. 2018b, *AJ*, **155**, 197
 Li, R., Youdin, A. N., & Simon, J. B. 2019, *ApJ*, **885**, 69
 Liu, B., Lambrechts, M., Johansen, A., Pascucci, I., & Henning, T. 2020, *A&A*, **638**, A88
 Lyra, W., & Umurhan, O. M. 2019, *PASP*, **131**, 072001
 McKinnon, W. B., Richardson, D. C., Marohnic, J. C., et al. 2020, *Sci*, **367**, aay6620
 Noll, K. S., Grundy, W. M., Chiang, E. I., Margot, J. L., & Kern, S. D. 2008, in *The Solar System Beyond Neptune*, ed. M. A. Barucci et al. (Tucson, AZ: Univ. Arizona Press), 345
 Parker, A. H., & Kavelaars, J. J. 2010, *ApJL*, **722**, L204
 Petit, J. M., Kavelaars, J. J., Gladman, B. J., et al. 2011, *AJ*, **142**, 131
 Petit, J. M., Kavelaars, J. J., Gladman, B. J., et al. 2017, *AJ*, **153**, 236
 Petit, J. M., & Mousis, O. 2004, *Icar*, **168**, 409
 Pike, R. E., Fraser, W. C., Schwamb, M. E., et al. 2017, *AJ*, **154**, 101
 Robbins, S. J., Singer, K. N., Bray, V. J., et al. 2017, *Icar*, **287**, 187
 Rucska, J. J., & Wadsley, J. W. 2021, *MNRAS*, **500**, 520
 Safronov, V. S. 1972, *Evolution of the Protoplanetary Cloud and Formation of the Earth and Planets* (Jerusalem: Keter Publishing House)
 Schäfer, U., Yang, C.-C., & Johansen, A. 2017, *A&A*, **597**, A69
 Schwamb, M. E., Fraser, W. C., Bannister, M. T., et al. 2019, *ApJS*, **243**, 12
 Shankman, C., Gladman, B. J., Kaib, N., Kavelaars, J. J., & Petit, J. M. 2013, *ApJL*, **764**, L2
 Shankman, C., Kavelaars, J., Gladman, B. J., et al. 2016, *AJ*, **151**, 31
 Sheppard, S. S., Udalski, A., Trujillo, C., et al. 2011, *AJ*, **142**, 98
 Simon, J. B., Armitage, P. J., Li, R., & Youdin, A. N. 2016, *ApJ*, **822**, 55
 Simon, J. B., Armitage, P. J., Youdin, A. N., & Li, R. 2017, *ApJL*, **847**, L12
 Singer, K. N., McKinnon, W. B., Gladman, B., et al. 2019a, *Sci*, **363**, 955
 Singer, K. N., Spencer, J. R., McKinnon, W. B., et al. 2019b, *AGUFM*, 2019, P331-3535
 Solontoi, M., Ivezić, Ž., Jurić, M., et al. 2012, *Icar*, **218**, 571
 Spencer, J. R., Stern, S. A., Moore, J. M., et al. 2020, *Sci*, **367**, aay3999
 Tegler, S. C., Romanishin, W., & Consolmagno, G. J. 2003, *ApJL*, **599**, L49
 van der Marel, N., van Dishoeck, E. F., Bruderer, S., et al. 2013, *Sci*, **340**, 1199
 Van Laerhoven, C., Gladman, B., Volk, K., et al. 2019, *AJ*, **158**, 49